

PAPER

Cite this: *RSC Adv.*, 2015, 5, 37006

Tip-based nanofabrication of arbitrary shapes of graphene nanoribbons for device applications†

 Huan Hu,^{‡*a} Shouvik Banerjee,^{‡bd} David Estrada,^f Rashid Bashir^{ade}
and William P. King^{acd}

Graphene nanoribbons (GNRs) have promising applications in future nanoelectronics, chemical sensing and electrical interconnects. Although there are quite a few GNR nanofabrication methods reported, a rapid and low-cost fabrication method that is capable of fabricating arbitrary shapes of GNRs with good-quality is still in demand for using GNRs for device applications. In this paper, we present a tip-based nanofabrication method capable of fabricating arbitrary shapes of GNRs. A heated atomic force microscope (AFM) tip deposits polymer nanowires atop a CVD-grown graphene surface. The polymer nanowires serve as an etch mask to define GNRs through one step of oxygen plasma etching similar to a photoresist in conventional photolithography. Various shapes of GNRs with either linear or curvilinear features are demonstrated. The width of the GNR is around 270 nm and is determined by the width of the deposited polymer nanowire, which we estimate can be scaled down to 15 nm. We characterize our TBN-fabricated GNRs using Raman spectroscopy and I - V measurements. The measured sheet resistances of our GNRs fall within the range of 1.65–2.64 k Ω \square^{-1} , in agreement with previously reported values. Furthermore, we determined the high-field breakdown current density of GNRs to be approximately 2.94 $\times 10^8$ A cm⁻². This TBN process is seamlessly compatible with existing nanofabrication processes, and is particularly suitable for fabricating GNR based electronic devices including next generation DNA sequencing technologies and beyond silicon field effect transistors.

Received 10th March 2015
Accepted 14th April 2015

DOI: 10.1039/c5ra04257g

www.rsc.org/advances

Introduction

The unique physical characteristics of graphene, a single atom thick sheet of sp² bonded carbon atoms arranged in a honeycomb lattice structure, was first predicted by Wallace *et al.*¹ and later confirmed by Geim *et al.*² Graphene has attracted wide interest in the scientific community for its unique properties like exceptionally high carrier mobility,^{3,4} extremely high current carrying capacity,^{5,6} high thermal conductivity⁷ and excellent mechanical stability.⁸ As silicon device scaling approaches its quantum limits, graphene nanostructures are being considered as possible replacements in micro and

nanoelectronics. Graphene nanoribbons (GNRs) are of particular interest as lateral quantum confinement of charge carriers creates a bandgap in graphene's density of states.^{9,10} GNRs also have potential applications in highly sensitive chemical sensing^{11,12} and nanopore-based DNA sequencing.^{13–15}

Although GNRs are very promising in all aforementioned applications, fabrication of good-quality GNRs that can be easily integrated for device fabrication remains a major challenge. Existing GNR fabrication methods can be categorized into two major classes: top-down and bottom-up. Top-down methods such as electron beam lithography (EBL)^{9,16} and Focused Ion Beam (FIB)^{17–19} are able to create arbitrary shapes of GNRs down to 20 nm resolution, but the process remains very expensive. Very importantly, the high energy beams can cause degradation of electronic properties of graphene.²⁰ Another top-down method, NanoImprint Lithography (NIL), is less expensive but still requires an expensive predefined mold and the design is limited by the mold. Bottom-up methods using chemical routes^{4,21–24} have lower cost and can produce GNRs with well-defined boundaries, but usually only produce very limited geometries of GNRs and lack precise placement and registry for subsequent device fabrication.

Here, we present a tip-based nanofabrication method (TBN)^{25,26} for fabricating GNRs, which is less expensive and easier to implement than all the existing top-down methods. No

^aDepartment of Electrical and Computer Engineering, University of Illinois at Urbana-Champaign, Urbana, IL 61801, USA. E-mail: huhuan99@gmail.com

^bDepartment of Materials Science and Engineering, University of Illinois at Urbana-Champaign, Urbana, IL 61801, USA

^cDepartment of Mechanical Science and Engineering, University of Illinois at Urbana-Champaign, Urbana, IL 61801, USA

^dMicro and Nanotechnology Laboratory, University of Illinois at Urbana-Champaign, Urbana, IL 61801, USA

^eDepartment of Bioengineering, University of Illinois at Urbana-Champaign, Urbana, IL 61801, USA

^fDepartment of Material Science and Engineering, Boise State University, USA

† Electronic supplementary information (ESI) available. See DOI: 10.1039/c5ra04257g

‡ Authors contributed equally.

vacuum environment is needed, no measurable damage is caused to the graphene during the process, and more excitingly this TBN method is seamlessly compatible with existing micro/nanofabrication methods, making it very promising for GNR device fabrication. In addition, the process is additive and only adds polymer nanowires where needed, therefore, resulting in much less polymer contamination than EBL which requires spin-coating of polymer resist covering the entire graphene surface.

Experiment – fabrication of nanostructures

Fig. 1 depicts the major steps for fabrication of graphene nanoribbons (GNRs) using TBN. A highly n-doped silicon substrate (resistivity = 0.005 Ω cm) with a 90 nm thick thermally grown silicon dioxide layer was used in this experiment. First, we fabricated micro-patterned metal electrodes consisting of a 2 nm thick titanium adhesion layer and 30 nm thick gold using conventional optical lithography and metal lift-off processes (Fig. 1(a)). Second, graphene was grown on copper by CVD process²⁷ and transferred onto the substrate using a process described previously⁵ (Fig. 1(b)). Raman spectroscopy measurements have indicated largely monolayer and some bilayer growth using this process.²⁸ The third step involves deposition of polystyrene nanowires (PS NWs) using a heated atomic force microscopy (AFM) tip (Fig. 1(c)). This step consists of two parts. The first part is to scan the sample surface using the AFM tip in non-heating mode to get the topography information about the microelectrodes. The second part is to specify the scan path of the heated AFM tip to deposit PS nanowires precisely across the microelectrodes. Subsequently the graphene unprotected by the PS nanowires is etched using oxygen plasma for 25 seconds (20 sccm O_2 , 90 W, 100 mTorr) and the remaining polystyrene (PS) residue is removed with acetone and isopropanol (Fig. 1(d)).

Graphene growth and transfer

Graphene is grown by chemical vapour deposition (CVD) on 1.4 mil copper foils purchased from Basic Copper. We used the

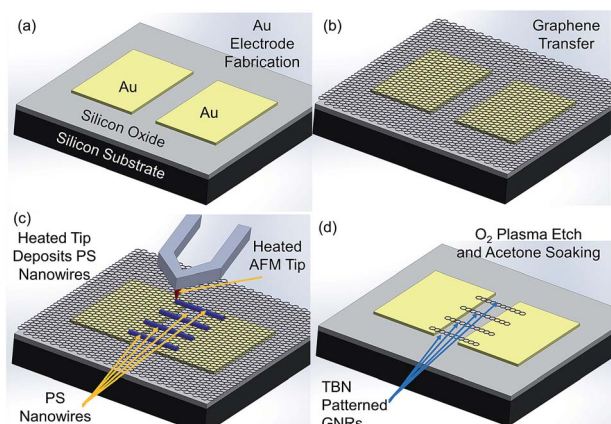


Fig. 1 Schematics illustrating major steps of GNR fabrication using TBN method with a heated AFM tip.

same growth process as previously described.^{27,28} After growth, both sides of the Cu are covered with graphene. We protect the graphene on the front side of the Cu foil by spin-coating a bilayer of PMMA (495 K A2 and 950 K A4) on top. And then we etch the unprotected graphene on the back side of the Cu foil using 30 seconds of oxygen plasma etching as previously described. Following this step only the front side of the Cu foil is covered with graphene due to the PMMA protection. We then etch the Cu foil overnight *via* wet etching with Cu etchant (Transene CE-100). The remaining PMMA/graphene film is then transferred to a 10% hydrochloride acid in deionized (DI) water solution to remove residual metal particles. After 10 min, the film is transferred to DI water rinse using a clean glass slide and the graphene is finally transferred to the sample with the fabricated metal Au microelectrodes ensuring that the PMMA/graphene film covers the region between the electrodes. The sample is then left to dry in air for about 1.5 h. The sample is heated at 50 $^{\circ}C$ for 5 min and then heated at 150 $^{\circ}C$ for 20 min to remove residual water and promote the adhesion of graphene film to the substrate. Finally, PMMA is removed by submerging the sample in a 1 : 1 methylene chloride/methanol solution for 45 min.

TBN step

The heated AFM tip we used in this work is made of a silicon double-armed micro-cantilever with a diamond-coated silicon tip at the free end developed in King's group.²⁹ Applying an electric current through the silicon micro-cantilever resistively heats up the tip. A closed-loop feedback circuit keeps the heated AFM tip at the desired temperature.^{30,31} The temperature of the tip is derived from the Stokes peak shift, measured using a Renishaw InVia Raman spectrometer. Heated silicon at different temperatures shifts the incident photon frequency differently and by measuring the frequency shift, we can calibrate the temperature of the heated AFM tip. This Raman microscope has a spatial resolution of 1 μm , an accuracy of around 1%, and a spectral resolution of 0.1 cm^{-1} .³²

In order to deposit PS NWs using the heated AFM tip, we first load the PS onto the tip by bringing the heated AFM tip into contact with a thin PS fiber under a stereo microscope. The thin PS fiber is manually prepared by inserting a metal wire into molten PS flakes (Polysciences Inc, polystyrene, molecular weight 50 000 atactic flakes) heated at 180 $^{\circ}C$ hotplate and slowly pulling the metal wire out. After molten PS flows onto the tip, we withdraw the tip from the fiber and turn off the heat. After loading the PS on the tip, we mount the tip into a commercial Asylum Research MFP-3D AFM and scan the tip along a programmed path with controlled temperature.

After adding the PS polymer, the tip might have an excess of polymer material resulting in the initial deposition of nanowires being very wide and thick. However, after several PS nanowire depositions, the width and thickness of the deposited PS become stable in a similar way as an ink pen deposits organic inks. We only deposit the PS NWs across the metal microelectrodes when the deposition is stable to ensure uniform width of PS NWs. Typically, one ink loading allows the tip to write about 2 hours before requiring additional polymer ink.³⁰

Results

Many factors affect the deposited PS NW geometries including tip temperature, tip scan speed, *etc.* Fig. 2(a) shows the 3D AFM topography image of the PS NWs deposited by the heated AFM tip on the graphene surface at different temperatures ranging from 170 °C to 190 °C with a step of 5 °C but all with the same tip speed of 150 nm s⁻¹. Fig. 2(b) summarizes the measured widths and heights of the PS NWs shown in Fig. 2(a). The width and height both increase almost linearly with increasing tip temperatures. Increasing temperature results in higher volume flow rate of molten polymer from the tip to the substrate, therefore forming PS NWs with larger width and height.

Fig. 3(a) shows the 3D AFM topography image of the PS NWs deposited at the same tip temperature of 175 °C but with different tip moving speeds. We use 100, 150, 200, 300, 400, 500 nm s⁻¹ tip moving speeds. Fig. 3(b) summarizes the measured widths and heights of the PS NWs shown in Fig. 3(a). Both PS width and height decrease with increasing tip speed since higher tip speed allows less time for the molten polymer to flow from the heated AFM tip to the graphene surface and therefore leads to formation of PS NWs with smaller width and height. Typical PS NW widths range between 400 nm and 600 nm for the current polystyrene material.

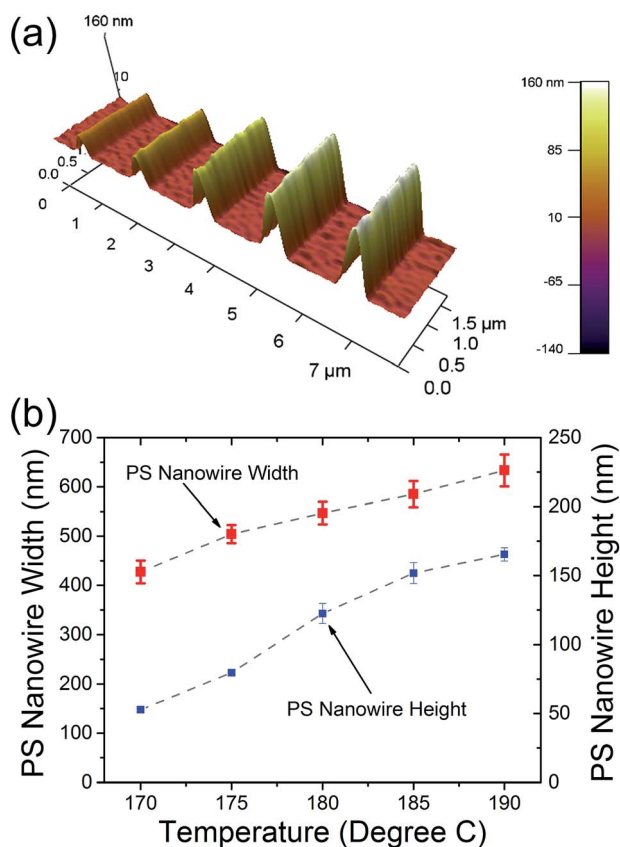


Fig. 2 (a) 3D AFM height image of PS NWs deposited using different temperatures but with the same tip speed of 150 nm s⁻¹; (b) measured widths and heights of PS NWs deposited using different temperatures but with the same tip speed of 150 nm s⁻¹.

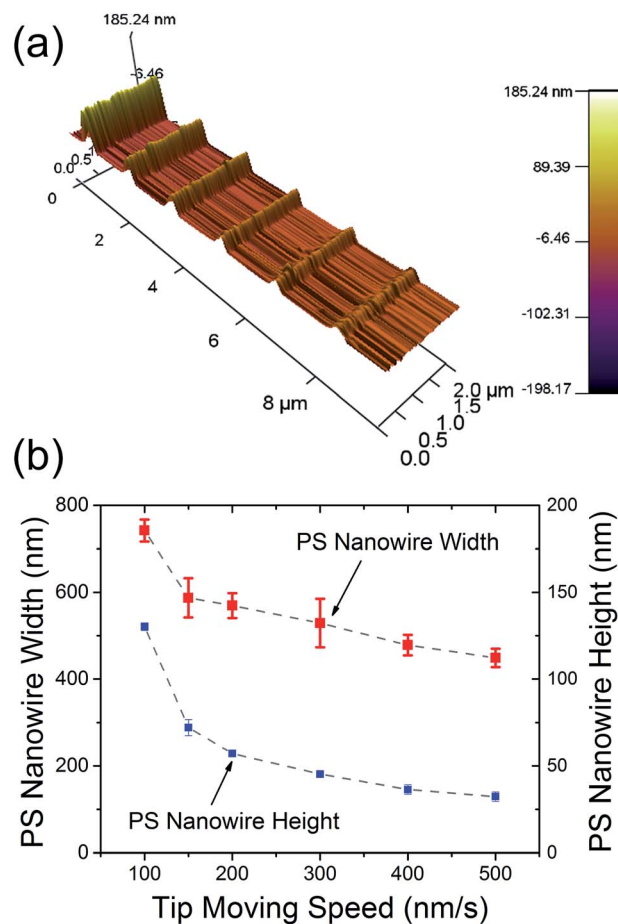


Fig. 3 (a) 3D AFM height image of PS NWs deposited using different tip speed but with the same temperature of 175 °C; (b) measured width and height of PS NWs deposited using different tip speeds but at the same tip temperature of 175 °C.

Fig. 4 shows the SEM images of GNRs with various shapes fabricated by our TBN method. Fig. 4(a) shows a circular GNR of 10 μm radius consisting of 32 small linear GNR segments. Fig. 4(b) shows the zoomed-in view of one segment of the circular graphene patterns. Fig. 4(c and d) shows a spiral-shaped GNR. Fig. 4(e) shows a wavy-shaped GNR and Fig. 4(f) shows an UIUC logo made of graphene. All the SEM images show that our TBN technique is highly versatile and able to fabricate arbitrary shapes of GNRs.

Fig. 5(a) shows an array of two linear GNRs across a pair of gold electrodes. Fig. 5(b) shows the zoomed-in view of a section of one linear GNR, showing a width of about 267 nm. Fig. 5(c) is the SEM image of an array of 4 linear GNRs and Fig. 5(d) shows the zoomed-in view of a section of one GNR, exhibiting a width about 290 nm. Fig. 5(e) shows an array of 8 linear GNRs across two gold electrodes. Fig. 5(f) shows the SEM image of the TBN-fabricated GNR in a tilted angle of 45°, clearly showing the is continuous from the Au electrode to the substrate. The width of the graphene pattern is slightly smaller than that of the PS NWs. This is because the PS NW is thicker in the middle and thinner at the edges. During oxygen plasma etching, PS at the edges is slightly etched and the underlying graphene also gets etched

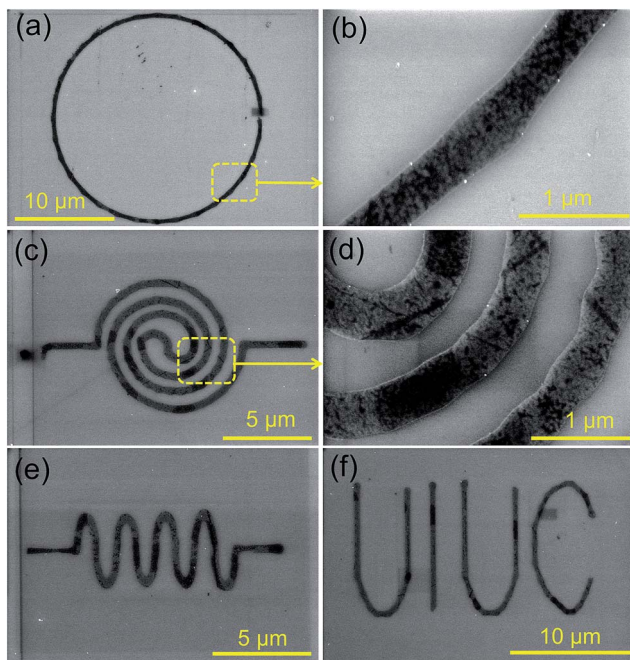


Fig. 4 SEM Images of different shapes of TBN-fabricated GNRs, demonstrating the fabrication flexibility of this TBN method. (a) A circular GNR with a radius of 10 μm ; (b) a zoomed-in view of a section of the circular GNR; (c) a spiral-shaped GNR; (d) a zoomed-in view of a section of the spiral-shaped GNR; (e) a wavy-shaped GNR; (f) GNR forming the shape of "UIUC" representing University of Illinois at Urbana-Champaign.

while PS in the middle survives the whole oxygen plasma etching and graphene underneath is not etched.

ESI Fig. S1† shows the representative Raman spectra of unpatterned CVD graphene and patterned GNRs. CVD graphene (black) is largely monolayer with very a small D-peak indicating largely defect free growth. The D-peak becomes more prominent in the circular patterned graphene (blue) which is approximately 450 nm in width and in the GNRs (red) which are approximately 250 nm in width.

Fig. 6(a) shows the I - V measurement of three different GNR arrays with 2, 4, 8 GNRs as shown in Fig. 5. All the ribbons are measured to have widths between 200–300 nm and the lengths are 10 μm . The voltage across the electrodes is swept from -1 to 1 V with a step of 40 mV. The resistances of the GNR arrays decrease with increasing numbers of ribbons. Based on the measured resistance, we estimated the sheet resistance of graphene using the following equation:

$$R_s = R \left(\frac{W}{L} \right) n \quad (1)$$

where, R_s is the sheet resistance, W is the average width of the graphene ribbon array, n is the number of ribbons in the array, L is the length of the electrode separation and R is the measured resistance.

For the 8 ribbon array, using an average measured width of 244 nm and length of 10 μm , we obtain a sheet resistance value of 1.65 $\text{k}\Omega \square^{-1}$. For the 4 ribbon and 2 ribbon array, the average

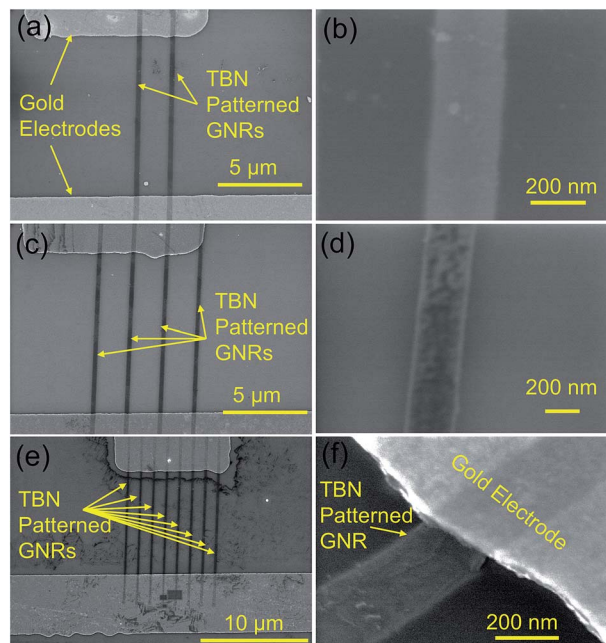


Fig. 5 SEM images of different arrays of TBN-fabricated GNRs across Au electrodes. (a) an array of 2 parallel GNRs across Au electrodes; (b) zoomed-in view of one GNR; (c) an array of 4 parallel GNRs across Au electrodes; (d) zoomed-in view of one GNR; (e) an array of 8 parallel GNRs across Au electrodes; (f) a zoomed-in view of intersection of GNR with a Au electrode.

GNR width was measured to be 276.7 nm and 267.0 nm indicating a high degree of uniformity for this process. The estimated sheet resistance values for these two arrays are 2.54 $\text{k}\Omega \square^{-1}$ and 2.64 $\text{k}\Omega \square^{-1}$ respectively. All the derived sheet resistance values agree well with reported values for such CVD grown graphene.^{33–36} The relative variation in sheet resistance could be attributed to some degree of bilayer and multilayer growth, along with contact resistance effects.

Fig. 6(b) shows the I - V measurements of GNRs after deposition of a layer of 8 nm thick Al_2O_3 dielectric layer on these GNR arrays. The measured resistances of the GNR arrays increase slightly upon deposition of the dielectric, which could be indicative of a reduction in doping levels caused by the dielectric deposition. This presence of the dielectric can reduce the physical adsorption of impurities such as adsorbed water and oxygen which makes the graphene p-doped.^{2,37} The Al_2O_3 atomic layer deposition (ALD) process has been reported to suppress such ambient air caused p-doping in graphene by a self-cleaning effect.³⁸ To achieve uniform nucleation and growth of the dielectric layer, we first deposit a 1.5 nm thick seed layer of aluminum,³⁹ which oxidizes spontaneously in air after removing the samples from the vacuum deposition chamber. We then deposit the additional Al_2O_3 dielectric layer using ALD.

We also investigated the gate dependence of the GNR channel in air. We measured the resistances of 4-ribbon and 8-ribbon arrays at each back-gate bias, while the back-gate, which in this case is the highly n-doped silicon substrate, was varied from -60 V to 60 V with a step size of 0.5 V. Fig. 7(a) shows the resistances

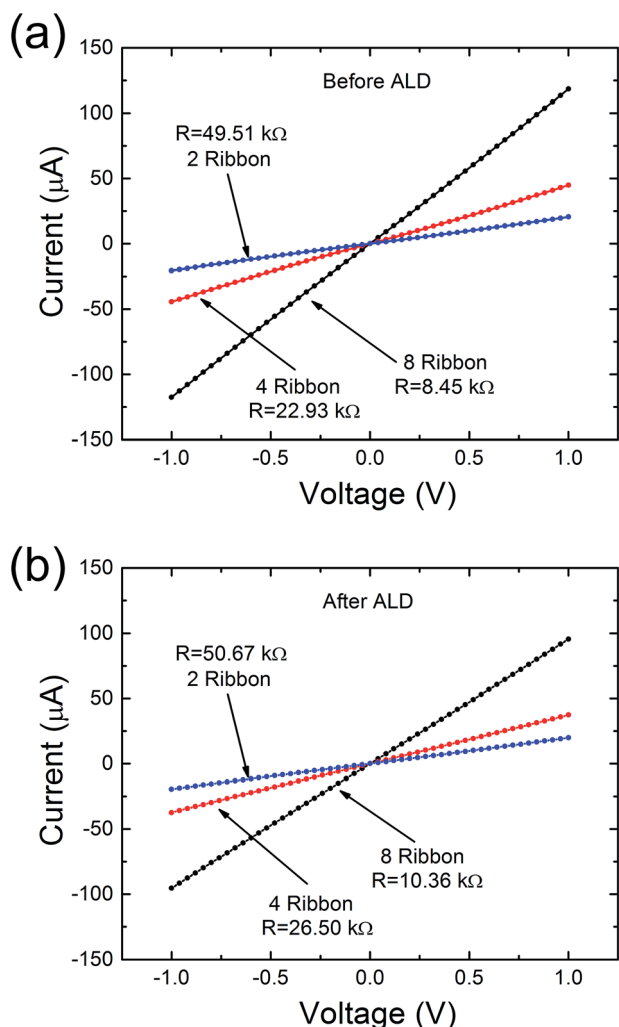


Fig. 6 Current–voltage measurement of devices with 2, 4, and 8 GNRs across the Au electrodes. The measured resistance of 2 GNRs is $49.51 \text{ k}\Omega$, 4 GNRs is $22.93 \text{ k}\Omega$, 8 GNRs is $8.45 \text{ k}\Omega$. Based on the measured GNR width and length, the estimated sheet resistance of graphene is $2.97 \text{ k}\Omega \square^{-1}$, $2.85 \text{ k}\Omega \square^{-1}$, and $1.65 \text{ k}\Omega \square^{-1}$, all of them are within literature-reported $1\text{--}6 \text{ k}\Omega \square^{-1}$ range. After ALD deposition of $8 \text{ nm Al}_2\text{O}_3$, the resistance of the 2 GNRs is $50.67 \text{ k}\Omega$, 4 GNRs is $26.50 \text{ k}\Omega$, 8 GNRs is $10.36 \text{ k}\Omega$. This is due to the reduction of p-doping levels of the GNRs, caused by the Al_2O_3 layer suppressing doping of graphene by ambient air.

of 4 ribbon and 8 ribbon array at different back-gate bias before ALD while Fig. 7(b) shows the results after ALD. For both the 8 ribbon and 4 ribbon arrays, a significant shift in Dirac points is found after ALD deposition of Al_2O_3 layer. Shifting of the Dirac point voltage to zero after ALD is consistent with a reduction of p-doping after the deposition process, and is observed for both the 8 ribbon and 4 ribbon arrays.

Finally, we also measured the high-field behavior of our TBN-fabricated GNRs to evaluate the current carrying capacity since graphene is potentially applicable for electrical interconnects.^{6,40} We have used the 2 ribbon GNR array (after Al_2O_3 dielectric deposition) for this particular experiment where a voltage is swept across the electrode until device failure. The results presented in Fig. 8 shows the stepwise breakdown of the

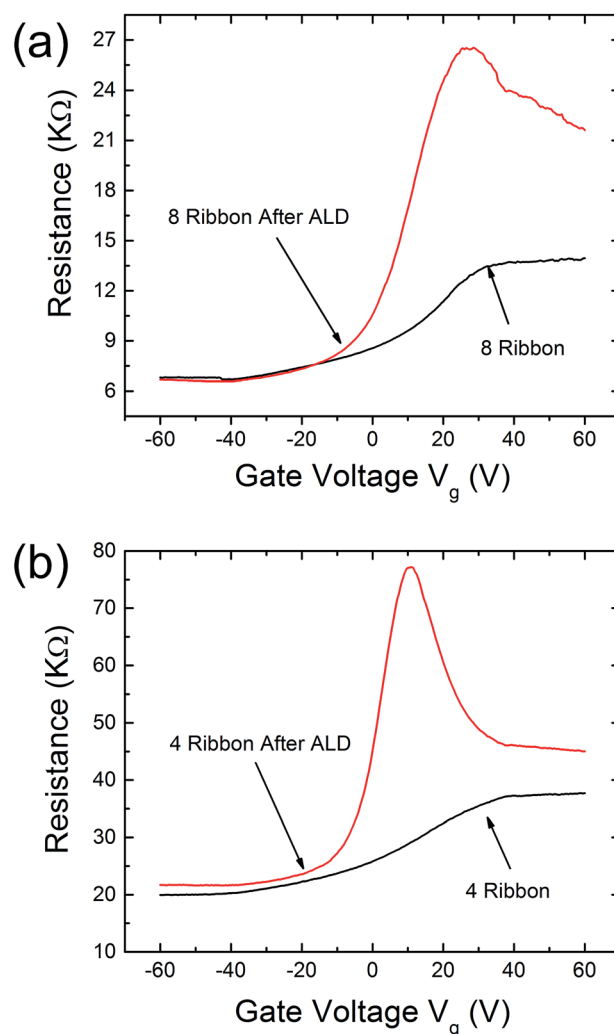


Fig. 7 Backgate measurement characteristics. (a) Resistances of 8 ribbon GNR array at different back gate bias before and after 8 nm thick ALD Al_2O_3 deposition; (b) resistances of 4 ribbon GNR array at different back gate bias before and after 8 nm thick ALD Al_2O_3 deposition. Variation of nanoribbon resistances are observed with varying gate voltages. On depositing the Al_2O_3 dielectric layer, the p-doping level decreases significantly as seen by increased GNR resistance and shifts in Dirac voltages both for 8 ribbon and 4 ribbon GNR array.

two individual ribbons. The breakdown manifests in significant reduction of the current in the ribbons. And the first breakdown current is about twice the value of the second breakdown current, further proving that it is caused by the breakdown of the graphene ribbons. The breakdown current density (assuming a monolayer thickness of graphene) is calculated to be $2.94 \times 10^8 \text{ A cm}^{-2}$, which compares well to literature reported values for both exfoliated and CVD grown graphene.^{6,41}

Discussions

Previously, we have demonstrated the fabrication of arbitrary silicon nanostructures using this TBN method as an additive nanolithography approach.⁴² In addition, we demonstrated

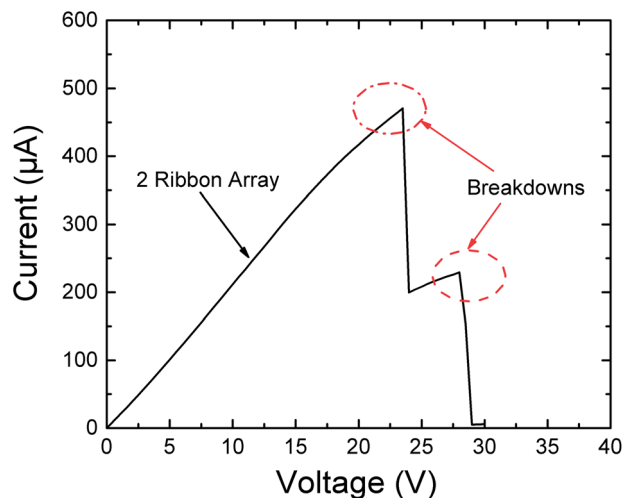


Fig. 8 Breakdown characteristics of 2 ribbon array. 2 breakdown levels are observed indicating the sequential breakdown of multiple ribbons. The calculated maximum current density is of the order of 10^8 A cm^{-2} which is consistent with literature-reported values.

seamless integration of this TBN method with conventional micro/nanofabrication methods by fabricating mechanical nano-resonators⁴³ and nanofluidic channels.⁴⁴ In all the previous work, PS NWs deposited by the heated AFM tip need to be thick enough to withstand strong plasma etching processes for silicon. Since PS NWs deposited usually have a fixed width/thickness ratio, it is very difficult to scale the width of the PS NW-protected silicon nanowires into smaller dimensions. However, in this work, we use PS NWs as an etch mask for patterning graphene and the etching of graphene only requires a very short period of oxygen plasma etching. A thinner polymer NW can withstand this etching, therefore, we have more room to reduce the width of the GNR fabricated using this TBN based method. Typically, 3 nm thick PS NWs suffice to protect the graphene during etching. Given the ratio of width to thickness being around 5, GNRs with 15 nm widths can be achieved by this TBN method, and are the subject of continuing studies. Further GNR width reduction might be possible with the help of chemical etching method.⁴⁵

The width of GNR is mainly determined by the width of the polymer nanowires mask deposited by the heated AFM tip. To reduce the width of GNR, we can use AFM tips with smaller tip radius, employ polymer materials with smaller viscosity and lower the substrate temperature.³⁰ ESI Fig. S2† shows an array of PMMA nanowires with the narrowest nanowires as narrow as 200 nm in width compared to 400 nm in width of PS nanowires. We used polymer material PMMA (average molecular weight 25 000) instead of polystyrene (average molecular weight 52 000) used for this work. Polymers with smaller molecular weights tend to be less viscous and therefore result in thinner nanowires.

Compared with other top-down GNR-fabrication methods, our TBN method has several distinctive advantages. First, the cost of AFM equipment can be as low as 100K US dollars compared with over 1 million dollar equipment required for

either EBL or FIB. Second, this TBN process is performed in ambient conditions, and no vacuum is required, which makes it possible to nanopattern samples prohibited in vacuum environments such as chemical or biological samples. Third, our TBN approach is additive and only deposits polymer where needed, thus resulting in much less contamination. Fourth, this TBN method has excellent capability of aligning nanoscale features to microscale features, a vital capability for nanoscale device integration. This is because this TBN method has built-in AFM imaging capability and can align features within the resolution of the piezoelectric stages in the AFM system, usually several nanometers, which compares favorably to the tens of nanometers alignment error for a normal EBL system.

Conclusions

In summary, we have presented the application of TBN with a heated AFM tip for fabricating arbitrary shapes of graphene nanostructures. This TBN method should have wide applications for fabrication of a wide variety of graphene nanostructures and should be easy to integrate with existing micro/nanofabrication process for development of new graphene devices. Moreover, our TBN method has precise control on position and size without expensive and complex electron beam lithography alignment processes. We fabricated arrays of long GNRs and obtained their transport properties which correlate well with devices fabricated by more complicated e-beam lithography processes on exfoliated graphene crystals. We also demonstrated the variation in transport properties in ambient conditions on deposition of a dielectric layer on the GNRs.

Acknowledgements

This work was supported by the NSF Center for Nano-Chemical-Electro-Mechanical Manufacturing Systems (NANO-CEMMS), Defense Advanced Research Projects Agency, National Institute of Health (R21 CA155863), Oxford Technologies U. K., National Science Foundation (DMR-0955959) and the Beckman Institute at the University of Illinois at Urbana-Champaign.

References

- 1 P. Wallace, *Phys. Rev.*, 1947, **71**, 622–634.
- 2 K. S. Novoselov, A. K. Geim, S. V. Morozov, D. Jiang, Y. Zhang, S. V. Dubonos, I. V. Grigorieva and A. A. Firsov, *Science*, 2004, **306**, 666–669.
- 3 K. I. Bolotin, K. J. Sikes, Z. Jiang, M. Klima, G. Fudenberg, J. Hone, P. Kim and H. L. Stormer, *Solid State Commun.*, 2008, **146**, 351–355.
- 4 S. Morozov, K. Novoselov, M. Katsnelson, F. Schedin, D. Elias, J. Jaszczak and A. Geim, *Phys. Rev. Lett.*, 2008, **100**, 016602.
- 5 S. Banerjee, J. Shim, J. Rivera, X. Jin, D. Estrada, V. Solovyeva, X. You, J. Pak, E. Pop, N. R. Aluru and R. Bashir, *ACS Nano*, 2012, **7**, 834–843.
- 6 A. Behnam, A. S. Lyons, M.-H. Bae, E. K. Chow, S. Islam, C. M. Neumann and E. Pop, *Nano Lett.*, 2012, **12**, 4424–4430.

- 7 A. A. Balandin, *Nat. Mater.*, 2011, **10**, 569–581.
- 8 C. Lee, X. Wei, J. W. Kysar and J. Hone, *Science*, 2008, **321**, 385–388.
- 9 M. Y. Han, B. Özyilmaz, Y. Zhang and P. Kim, *Phys. Rev. Lett.*, 2007, **98**, 206805.
- 10 L. Ma, J. Wang and F. Ding, *ChemPhysChem*, 2013, **14**, 47–54.
- 11 J. L. Johnson, A. Behnam, S. J. Pearton and A. Ural, *Adv. Mater.*, 2010, **22**, 4877–4880.
- 12 A. N. Abbas, G. Liu, B. Liu, L. Zhang, H. Liu, D. Ohlberg, W. Wu and C. Zhou, *ACS Nano*, 2014, **8**, 1538–1546.
- 13 F. Traversi, C. Raillon, S. M. Benameur, K. Liu, S. Khlybov, M. Tosun, D. Krasnozhan, A. Kis and A. Radenovic, *Nat. Nanotechnol.*, 2013, **8**, 939–945.
- 14 A. Girdhar, C. Sathe, K. Schulten and J.-P. Leburton, *Proc. Natl. Acad. Sci. U. S. A.*, 2013, **110**, 16748–16753.
- 15 K. K. Saha, M. Drndic and B. K. Nikolic, *Nano Lett.*, 2012, **12**, 50–55.
- 16 Z. Chen, Y.-M. Lin, M. J. Rooks and P. Avouris, *Phys. E*, 2007, **40**, 228–232.
- 17 D. C. Bell, M. C. Lemme, L. A. Stern, J. R. Williams and C. M. Marcus, *Nanotechnology*, 2009, **20**, 455301.
- 18 J.-F. Dayen, A. Mahmood, D. S. Golubev, I. Roch-Jeune, P. Salles and E. Dujardin, *Small*, 2008, **4**, 716–720.
- 19 M. C. Lemme, D. C. Bell, J. R. Williams, L. A. Stern, B. W. H. Baugher, P. Jarillo-Herrero and C. M. Marcus, *ACS Nano*, 2009, **3**, 2674–2676.
- 20 D. Teweldebrhan and A. A. Balandin, *Appl. Phys. Lett.*, 2009, **94**, 013101.
- 21 L. Gao, W. Ren, B. Liu, Z.-S. Wu, C. Jiang and H.-M. Cheng, *J. Am. Chem. Soc.*, 2009, **131**, 13934–13936.
- 22 L. Ci, Z. Xu, L. Wang, W. Gao, F. Ding, K. F. Kelly, B. I. Yakobson and P. M. Ajayan, *Nano Res.*, 2008, **1**, 116–122.
- 23 S. S. Datta, D. R. Strachan, S. M. Khamis and A. T. C. Johnson, *Nano Lett.*, 2008, **8**, 1912–1915.
- 24 X. Li, X. Wang, L. Zhang, S. Lee and H. Dai, *Science*, 2008, **319**, 1229–1232.
- 25 A. A. Tseng, S. Jou, A. Notargiacomo and T. Chen, *J. Nanosci. Nanotechnol.*, 2008, **8**, 2167–2186.
- 26 R. Garcia, A. W. Knoll and E. Riedo, *Nat. Nanotechnol.*, 2014, **9**, 577–587.
- 27 X. Li, W. Cai, J. An, S. Kim, J. Nah, D. Yang, R. Piner, A. Velamakanni, I. Jung, E. Tutuc, S. K. Banerjee, L. Colombo and R. S. Ruoff, *Science*, 2009, **324**, 1312–1314.
- 28 B. M. Venkatesan, D. Estrada, S. Banerjee, X. Jin, V. E. Dorgan, M.-H. Bae, N. R. Aluru, E. Pop and R. Bashir, *ACS Nano*, 2011, **6**, 441–450.
- 29 P. C. Fletcher, J. R. Felts, Z. Dai, T. D. Jacobs, H. Zeng, W. Lee, P. E. Sheehan, J. A. Carlisle, R. W. Carpick and W. P. King, *ACS Nano*, 2010, **4**, 3338–3344.
- 30 J. R. Felts, S. Somnath, R. H. Ewoldt and W. P. King, *Nanotechnology*, 2012, **23**, 215301.
- 31 S. Somnath, H. J. Kim, H. Hu and W. P. King, *Nanotechnology*, 2014, **25**, 014001.
- 32 J. Lee, T. Beechem, T. L. Wright, B. A. Nelson, S. Graham and W. P. King, *J. Microelectromech. Syst.*, 2006, **15**, 1644–1655.
- 33 G. Fisichella, S. Di Franco, P. Fiorenza, R. L. Nigro, F. Roccaforte, C. Tudisco, G. G. Condorelli, N. Piluso, N. Spartà and S. L. Verso, *Beilstein J. Nanotechnol.*, 2013, **4**, 234–242.
- 34 A. Salehi-Khojin, D. Estrada, K. Y. Lin, M.-H. Bae, F. Xiong, E. Pop and R. I. Masel, *Adv. Mater.*, 2012, **24**, 53–57.
- 35 W.-C. Yen, Y.-Z. Chen, C.-H. Yeh, J.-H. He, P.-W. Chiu and Y.-L. Chueh, *Sci. Rep.*, 2014, **4**, 4739.
- 36 X. Li, Y. Zhu, W. Cai, M. Borysiak, B. Han, D. Chen, R. D. Piner, L. Colombo and R. S. Ruoff, *Nano Lett.*, 2009, **9**, 4359–4363.
- 37 L. Liu, S. Ryu, M. R. Tomasik, E. Stolyarova, N. Jung, M. S. Hybertsen, M. L. Steigerwald, L. E. Brus and G. W. Flynn, *Nano Lett.*, 2008, **8**, 1965–1970.
- 38 L. Zheng, X. Cheng, D. Cao, Z. Wang, C. Xia, Y. Yu and D. Shen, *Appl. Phys. Lett.*, 2014, **104**, 023112.
- 39 S. Kim, J. Nah, I. Jo, D. Shahrjerdi, L. Colombo, Z. Yao, E. Tutuc and S. K. Banerjee, *Appl. Phys. Lett.*, 2009, **94**, 062107.
- 40 A. D. Liao, J. Z. Wu, X. Wang, K. Tahy, D. Jena, H. Dai and E. Pop, *Phys. Rev. Lett.*, 2011, **106**, 256801.
- 41 R. Murali, Y. Yang, K. Brenner, T. Beck and J. D. Meindl, *Appl. Phys. Lett.*, 2009, **94**, 243114.
- 42 H. Hu, P. K. Mohseni, L. Pan, X. Li, S. Somnath, J. R. Felts, M. A. Shannon and W. P. King, *J. Vac. Sci. Technol., B*, 2013, **31**, 06FJ01.
- 43 H. Hu, H. Cho, S. Somnath, A. F. Vakakis and W. P. King, *Nanotechnology*, 2014, **25**, 275301.
- 44 H. Hu, Y. Zhuo, M. E. Oruc, B. T. Cunningham and W. P. King, *Nanotechnology*, 2014, **25**, 455301.
- 45 X. Wang and H. Dai, *Nat. Chem.*, 2010, **2**, 661–665.